Additive Manufacturing 35 (2020) 101263

Contents lists available at ScienceDirect

Additive Manufacturing

journal homepage: www.elsevier.com/locate/addma

Research Paper

Pulsed mode selective laser melting of porous structures: Structural and thermophysical characterization

Davoud Jafari[a,*], Wessel W. Wits[b], Tom H.J. Vaneker[a], Ali Gökhan Demir[c], Barbara Previtali[c], Bernard J. Geurts[d], Ian Gibson[a]

[a] Faculty of Engineering Technology, University of Twente, P.O. Box 217, 7500 AE, Enschede, the Netherlands
[b] Thales Netherlands, P.O. Box 42, 7550 GD, Hengelo, the Netherlands
[c] Department of Mechanical Engineering, Politecnico di Milano, Via La Masa 1, 20156, Milan, Italy
[d] Faculty of Electrical Engineering, Multiscale Modeling and Simulation, University of Twente, P.O. Box 217, 7500 AE, Enschede, the Netherlands

ARTICLE INFO

Keywords:
Selective laser melting
Porous structure
Wettability
Capillary performance
Thermal conductivity

ABSTRACT

In this paper, the potential of selective laser melting (SLM) of stainless steel CL 20ES powder was investigated with a focus on controlled fabrication of porous structures with strongly reduced pore sizes, i.e. feature sizes significantly below conventional minimum SLM feature sizes. By controlling laser scan properties interacting with the powder bed directly, porous structures can be generated by selectively sintering powder particles. A wide range of porous samples was manufactured following this strategy, aiming to increase porosity while keeping pore sizes low. The effect of process parameters, including laser power and focal point positioning, was evaluated for a fibre laser operated in pulsed wave (PW) emission mode. The first part of this study focuses on characterization of key porous structure properties, i.e., porosity, average mass density, average pore sizes and structures at microscopic scales. The second part deals with the influence of porosity and pore sizes on thermal and fluid properties, i.e., the effective thermal conductivity (ETC) and wettability. We have quantified the directional dependence (build direction plane and scan direction plane) off the structural and thermophysical properties of porous structures. For a range of porosities and pore sizes, we have observed that porosity and surface morphology influence the thermal properties and contact angle of droplets on the printed surface. Thermal conductivity was measured and the associated analysis was compared with available models and correlations in literature. The average thermal conductivity of fabricated porous structures was determined between 6 – 14 W/m K and found to be a function of porosity. Furthermore, the capillary wicking performance of additively manufactured stainless steel porous structures having an average pore radius from 9 to 23 μm was determined.

1. Introduction

Porous structures find their place in several applications, such as in heat pipes, air-conditioning systems, gas turbines, electronics cooling, chemical reactors, fuel cells, thermal energy storage systems, batteries and many more [1–3]. Rapidly evolving additive manufacturing (AM) technologies have become a focus of interest in the field of fabrication of porous structures with controlled properties [4]. One of the principal advantages of additively manufactured porous structures is the possibility of designing the microstructures and producing a desired (complex) freeform geometry. So far, in metal AM processes porosity has been primarily regarded as a process artefact to be reduced so that correct mechanical properties can be maintained [5]. Indeed, lattice structures as well as metallic foam structures have been designed and manufactured, which exploit the geometrical flexibility of AM.

The use of materials with designed geometrical porosity has been considered primarily in medical applications [5] to allow for tissue ingrowth. Other recent works involve porous media for heat pipes [6–9], for loop heat pipes in light emitting diode lamp applications [10], for the enhancement of heat transfer in pool boiling [11] and for advanced electrochemical flow reactors [12]. These studies show that performance of heat transfer devices constructed via AM is better than that of devices manufactured by conventional methods. The dimensional range of pores obtained in these studies reflects the geometrical capabilities of the processes. One of the most scientifically researched and industrially applied metal AM processes is selective laser melting

* Corresponding author.
E-mail addresses: jafariidavoud@gmail.com, davoud.jafari@utwente.nl (D. Jafari).

https://doi.org/10.1016/j.addma.2020.101263
Received 6 December 2019; Received in revised form 13 April 2020; Accepted 15 April 2020
Available online 11 May 2020
2214-8604/ © 2020 The Author(s). Published by Elsevier B.V. This is an open access article under the CC BY license (http://creativecommons.org/licenses/BY/4.0/).

(SLM). This process reaches among the smallest feature sizes, in which pore dimensions are limited to a range of 50–150 μm, depending on the granularity of the metal powder, and the process itself (laser spot diameter, heat affected zone, etc.). To achieve considerably smaller pore sizes, the SLM process needs to be operated in a new parameter regime outside conventional process design strategies. We dedicate this study to the manufacturing and characterisation of these new porous structures.

AM has been used successfully for the production of porous structures of sufficiently large features in the millimetre range. To the best of the authors' knowledge, there is no example of successfully fabricated porous structures with uniformly small pore sizes in combination with high porosity. As a matter of fact, a reduction of pore sizes well into the submillimetre range for metal AM processes requires enhanced process knowledge and control to enable users to switch from a full-melting process to a sintering-based process in which interconnected 'strands' form controlled porous structures in the dimensional range of the metallic powders, i.e., with features of 15–60 micrometres. This is the focus of this paper.

The main aim is to develop porous structures with small pore sizes without unduly decreasing the porosity – so, we wish to achieve porous structures with a very large number of very small pores. Such a combination has not yet been realised by AM methods. The production of porous structures has been considered with various methods in the past. Among these, the most common is powder sintering [13]. We focus on AM processes based on metal powder bed fusion, such as SLM, providing control over the pore size, distribution and porosity. The objective of this study is to develop a sintered-like porous structure using SLM rather than using a conventional pressurized mould and heat source. SLM is capable of printing porous lattice structures for which porosity ranges from about 20 % in the case of 300 μm pore sizes to 60 % in the case of 500 μm pore size samples [6]. In previous work, we applied SLM as fabrication method for the development of a heat pipe system using computer-aided design (CAD) features to provide the porous structures [8,9,14]. This work has demonstrated higher capillary performance [9] and improved phase change heat transfer characteristics [8] than that is possible with traditional fabrication processes. We achieved a porosity of 46 % for an additively manufactured porous structure with an average pore size of 216 μm [9]. Current aim of this study is to significantly improve this state of the art by increasing the porosity, while decreasing the average pore size. Commercial computer-aided manufacturing (CAM) software, developed to build solid features from CAD representations, cannot generate a suitable laser scan pattern, parameters and strategy for this. A variety of deposition strategies exists (up-skin, down-skin, core, and sidewalls), focusing on creating a geometry with minimal porosity, low surface roughness, high deposition speeds, etc. [5]. A new strategy needs to be developed that allows for the construction of part sections with small pores, high porosity and adequate levels of mechanical strength. Hence, for this study the laser scanner in our experimental set-up is controlled directly beyond the scope of a traditional CAM environment.

For industrial SLM systems and even for laser processing in general, in terms of the laser energy emission mode, a primary distinction can be employed: continuous wave (CW) emission [15,16] and pulsed wave (PW) emission [17]. The pulsed emission mode is accomplished by modulating the laser emission using fast switching of the electrical current for the pumping diodes. Compared to CW, PW emission provides more versatile laser power operation by regulating the pulse overlap in the scanning direction and between the adjacent scan lines [17]. We recently showed that PW operation can be highly beneficial to obtain porous structures with specific microstructures as these small features were found to be sensitive to the energy density of the laser [17,18]. Therefore, in this study for sintering-like metal powder processing by SLM, the PW emission mode is investigated. Instead of building pre-defined porous structures, process parameters were varied systematically to only (partially) sinter metal powder particles within the powder bed instead of fully melting the particles. Such additively manufactured porous structures offer an alternative to the currently available sintered porous structures particularly beneficial for two-phase flow devices, as well as in cases where high capillary pumping to enhance heat and mass transfer is required, e.g., fuel cells, batteries, energy storage systems, etc. This study aims at delivering a new genre of freeform porous structures having high capillary pumping and tailored compositions.

The objectives of this paper are as follows:

1 From an engineering point of view, additively manufactured porous structures are fabricated by employing the PW emission mode for SLM. To date, there are no successful studies reported in literature that aim to reduce the pore size of porous structures using PW emission. We consider different laser parameters influencing the pore size and overall porosity, specifically looking to minimize the pore size while retaining the porosity effectively constant.
2 There is very little research available on the thermo-fluid properties of additively manufactured components and their relationship to process parameters compared to extensive literature on mechanical relationships. Thermophysical properties of fluids such as thermal conductivity, control the process of heat flow through a component, and are therefore crucial to understanding the performance of the part in an engineering application in which heat generation and heat transfer are important considerations. Similarly, wettability of a material's surface is an important property. Like mechanical properties [19], it is reasonable to expect that thermal conductivity and wettability will be affected by the direction of manufacturing AM parts, i.e., build direction and laser scan direction. We examined additively manufactured porous structures with different physical properties and thermophysical characteristics for different directions. Capillary performance and thermal analysis studies were performed on the porous structures by measuring the physical properties of wettability (i.e., contact angle), flow property measurements (i.e., porosity and pore radius), and porous structures' thermal conductivity.

This paper is organized as follows. In Section 2, we shortly introduce the problem description regarding porous structures for important energy conversion systems. In Section 3, a short description of SLM to fabricate porous structures is presented, including details of an SLM system operating with a PW fibre laser. The experimental design is also described. Porous structures characterization methods and the experimental setup to determine thermal and fluid transport properties are presented in Section 4. In Section 5, results of the characterization of the material itself, i.e., porosity, mass density, pore size and fabricated microstructures are discussed. The focus is on the influence of the porosity and pore size on the thermal conductivity and wettability. We discuss the results, relating the process parameters to thermo-fluid properties in Section 6. Finally, in Section 7, conclusions are drawn, and perspectives are discussed.

2. Thermophysical properties of fluids through porous structures

Developments in fluid and thermal transport through porous structures are critical to improve heat transfer systems in many technological fields, e.g., heat pipes [8]. In fact, the transport of complex multiphase fluids, conductive and convective heat transfer as well as surface interaction of porous structures (pores) depend on various parameters including microstructural and surface properties [20]. One of the areas of research in the development of new materials includes finding a way of achieving optimal macroscopic performance of porous structures (i.e., thermal conductivity) through their surface (i.e., wettability) and internal (i.e., porosity) properties. In particular, highly porous structures combine low density with unique thermophysical properties which can be modified in accordance with the intended

application and functionality [1,8,9,21,22].

The porous structure acts as a pump for fluid flow by creating capillary pressure within the (micro)pores for capillary-driven heat pipes. The desired balance between conflicting characteristics of the porous structures is very important for this application and many other energy conversion applications, including:

(a) High capillary driving force, which is accomplished by reducing the pore radius – Based on the Young-Laplace equation, the capillary pressure is defined as the pressure drop across a channel needed to transport a unit mass flow of liquid and is expressed as:

$$\Delta P_c = \frac{2\sigma\, cos\theta}{r_p} \tag{1}$$

where, σ is the surface tension coefficient of the liquid, θ is the equilibrium contact angle and r_p is the pore radius [23]. According to Eq. (1), the capillary performance of the porous structures is also characterized by the surface wettability. In fact, the wettability of the solid surface is an important property and can be determined by the contact angle of a droplet on the surface. Droplet spreading behaviour on a porous structure's surface however differs from spreading on a solid surface. Droplet spreading on a porous surface is a combination of (i) the spread of the droplet over the surface and (ii) simultaneous capillary penetration [24]. Hence, it is much more challenging to understand the wetting of porous surfaces compared to solid surfaces. This depends on several factors, including conditions of material and surface, porosity, roughness and liquid properties [25]. Penetration within a porous medium and spreading on a porous surface with uniform pore structures have been studied theoretically [25–31]. However, little attention has been paid to the experimental evaluation of drop impact on porous structures [32,33]. The proposed technique to measure the liquid-solid contact angle on additively manufactured porous structures is described in subsection 3.3.2.

(b) Low hydraulic resistance attained with high porosity and maximized pore radius – The pressure drop for one-dimensional axial flow through a porous medium, defined by Darcy's law, shows that the flow resistance dependence on the permeability as:

$$\frac{dp}{dx} = -\frac{\mu_l \dot{m}_l}{\rho_l A_w K} \tag{2}$$

where K is permeability, μ_l and ρ_l are liquid viscosity and density, respectively, $\dot{m}_l$ is the mass flow rate and A_w is the porous media's cross sectional area. Permeability (K), which has an affect the transportability of fluid through a porous medium, is expressed based on the Kozeny-Carman equation [23]:

$$K = \frac{4r_p^2\varepsilon^2}{S(1-\varepsilon)^2} \tag{3}$$

where, ε is the porosity and S is the shape coefficient. The shape coefficient is reported to be around 105 for an additively manufactured porous structure [9]. The unavoidable trade-off between capillary pressure and permeability determines the optimal length-scale within the porous structure for a given fluid flow rate. Such a capillary limitation describes one of the potential physical limitations of two-phase flow.

(c) A high effective thermal conductivity (ETC) results in a small drop in temperature throughout the system, which is beneficial to overall transport characteristics. ETC is determined on the basis of the thermal conductivity of both solid and fluid materials that constitute the porous media [34]. In fact, the effective thermal characteristics of additively manufactured porous structures are directly related to manufacturing parameters that determine the resulting porosity and pore-size distribution [1,35,36]. The porous structures of this study range from very low porosity, i.e., almost fully molten powder, to high porosity, i.e., sintered-like powder. Several studies have been reported on theoretical methods (often based on a simplified unit cell structure) and empirical correlations for predicting ETC in porous structures [34]. Examples of such contributions are summarized in Table 1. In order to facilitate comparisons with the experimental results obtained in this study, these models and correlations are presented here. While there are only a few thermal conductivity studies for additively manufactured materials [7,37], there is no study on the thermal properties of metal AM looking into the thermal properties versus build direction and scan direction planes. One of the objectives of this research is to establish the relationship between ETC of additively manufactured porous samples and manufacturing parameters. Moreover, this is also an assessment of the validity of existing literature models and correlations.

Table 1
Review of porosity-dependent models and theories for ETC prediction (where ε is porosity, k_s and k_f are solid and fluid thermal conductivity).

Model – description	Correlations
Parallel (upper limit for ETC) [34]	$ETC = \varepsilon k_f + (1-\varepsilon)k_s$
Lower Maxwell (lower limit for ETC) [34]	$ETC = k_f \frac{2\varepsilon + \left(\frac{k_s}{k_f}\right)(3-2\varepsilon)}{3-\varepsilon+\varepsilon\left(\frac{k_s}{k_f}\right)}$
Upper Maxwell (upper limit for ETC) [34]	$ETC = k_f \frac{2\left(\frac{k_s}{k_f}\right)^2(1-\varepsilon)+(1+2\varepsilon)\left(\frac{k_s}{k_f}\right)}{1-\varepsilon+(2+\varepsilon)\left(\frac{k_s}{k_f}\right)}$
Simplified series-parallel model and the Misnar model [39]	$ETC = (1-\varepsilon^{2/3})k_s$
Scaling relation [39]	$ETC = (1-\varepsilon)^n k_s$

(d) High capillary performance resulting in high maximum heat transfer capacity – The capillary limit of a two-phase device is directly related to (i) figure of merit of the working liquid, (ii) geometrical dimensions, and (iii) capillary performance (K/r_{eff}) taking into account competing factors: permeability (K) and effective pore radius (r_{eff}). The latter r_{eff} is the effective pore radius ($r_p/cos\ \theta$). In porous structures there are two important properties: 1) the capillary pressure scaling inversely with pore radius (Eq. (1)), while 2) the permeability scales with the square of the pore radius (Eq. (3)) [13]. Desired characteristics of porous structures for two-phase devices include (i) high capillary pressure – achieved by a small pore radius – and (ii) high permeability – achieved by a high porosity and pore radius. These characteristics are conflicting variables, and in order to optimize the performance, design parameters must be carefully selected. A key parameter, the capillary performance defined as the ratio of permeability to effective capillary pore radius K/r_{eff} [9,38], is discussed in this paper.

In summary, the principal objective of this paper is to understand fluid and heat transport in porous structures developed by SLM and thereby improve design and performance capabilities. These parameters directly impact thermophysical properties and capillary performance [9]. The first step in understanding the SLM processing to prototype suitable specimens, as described in the following section.

3. Porous structures manufacturing by SLM

First the SLM approach to 3D metal printing is discussed and subsequently the parameter study that was undertaken is formulated. SLM technology is a particularly suitable AM method compared to traditional production methods when complex freeform geometries are required. Most of the SLM systems that are commercially available work

with CW lasers. As a consequence, substantial effort has been directed toward producing bulk (solid) objects, preferably without (significant) voids (i.e., porosity) through optimizing CW system parameters. Considerably less effort has been given to high-porosity metal components incorporating levels of porosity achieved by a sintering process alone. As a matter of fact, the current state of the art has been focused on reducing this type of porosity in order to improve the mechanical properties of printed parts. However, using the great flexibility of fibre lasers, commonly employed in SLM systems, one can also consider switching the working conditions from full melting to sintering and vice versa. Energy density and PW emission can be varied considerably by power modulation – we exploit this modulation to tailor the processing conditions such that desired porous and fully dense zones are obtained in one part [40].

In order to obtain a desirable porous structure by SLM, the PW operation should be understood in some detail. Laser power (P) and pulse duration (τ), in general, determine the energy transfer into the powder bed. The focal position (f) controls the beam focal point relative to the surface of the powder bed, hence controlling the (de)focusing distance. A negative focal point for the present system refers to a laser spot above the surface of the powder bed, whereas a positive focal point refers to a spot below the surface of the powder bed. Apart from PW emission, point distance (dx), hatch distance (dh) and layer thickness (z) are also important parameters. During the process of powder bed fusion, laser energy density is considered a key factor [5] to define the energy applied per unit volume of powder bed as it affects the performance of the produced component. In this study, laser energy density (E) is reformulated to express PW emission as:

$$E = \frac{P\tau}{dx\, dh\, z} \tag{4}$$

In SLM the use of a defocused beam has been studied rarely [41,42]. Indeed, the effect of defocusing is effectively changing the beam spot size. Hence, the fluence parameter, which expresses the energy density at the peak of an ideal beam with a Gaussian distribution, changes. Fluence can be expressed as [43]:

$$F = \frac{2P\tau}{\pi w_s^2} \tag{5}$$

where, w_s is the beam radius.

It is a crucial task to identify optimal process parameters. However, during the laser melting process, relevant parameters may induce a complex combined effect; thus, a systematic design of experiment is required. The porosity/mass density variation can best be characterized when some parameters are kept constant. In this study, the experiment was designed based on a low-to-(relatively) high energy density, influenced by laser power and focal position. As output parameters the porosity and pore size of the fabricated porous structures are analysed.

A Renishaw AM250 SLM system was used for the experimental work using an active fibre laser with a maximum power of 200 W. The optical chain consisted of a galvanometric scanner with integrated z-axis positioner, which enables the beam's focal position to be controlled. Prior to test part fabrication, air was pumped out of the build chamber and filled with argon as a shielding gas. The reduced oxygen content prevents the powder from oxidizing. The Renishaw AM250, equipped with PW emission, splits scanning into stationary exposure for a short time followed by point distance traversal, so-called spot-to-spot formation. The laser pulsates along the scan direction with an uninterrupted motion in order to release a certain duration of pulses with a determined point distance between them. The laser jumps to the adjacent line at the end of every scanned line. The process continues until a single layer is thoroughly screened, after which the re-coater deposits a new layer of powder. At each layer the scan direction is varied by 67°. The SLM system was equipped with a reduced build volume platform capable of producing small-sized specimen in a build volume of 78 × 78 × 50 mm^3.

Table 2
Details of the experimental conditions.

Fixed parameters	
Layer thickness, z	50 µm
Point distance, dx	60 µm
Hatch distance, dh	110 µm
Pulse duration, τ	80 µs
Varied parameters	
Power, P	60; 80; 100; 120; 140; 160; 180; 200 W
Focal point, f	0; 3; 6 mm

The experimental design consists of 24 cases, composed of three (focal point f) by eight (laser power P) settings, fabricating a cubic porous structure of 5 × 5×5 mm^3 for each setting. Table 2 lists fixed and varied parameters used in the experiment. The point distance (dx), hatch distance (dh) and powder layer thickness (z) were 60 µm, 110 µm and 50 µm, respectively. Laser power was adjusted from 60 to 200 W to have an energy density ranging from 14.5–48.5 J/mm^3. The theoretical beam radius at the given configurations was estimated using a Gaussian beam propagation [44] of 38 µm, 145 µm, and 320 µm for the 0, 3, 6 mm focal positions, respectively. In this configuration, the fluence ranged between 3 and 724 J/cm^2. Fig. 1 shows the relationship between energy density and fluence used in the experimental conditions. It can be seen that the same energy density over the layer was delivered with different fluence values indicating different beam intensities. During the experiments no border scans, up-skin or down-skin strategies were employed. Fig. 2 shows an image of the fabricated porous cubes including the parameter variation.

4. Experimental apparatus and characterization

In this section, the experimental methods used to characterize thermal and fluid transport properties of the set of porous cubes, as displayed in Fig. 2, are described.

To evaluate the effect of pore radius and porosity on the capillary performance, wettability and thermal performance, the additively manufactured porous structures are first examined using scanning electron microscopy (SEM) (for as-fabricated samples), optical microscopy (for polished samples), volumetric mass density and Archimedes testing for pore size and porosity investigations. Afterwards, thermal conductivity and capillary performance are evaluated by an in-house setup and contact angle measurement device, respectively. The experimental setup and approach is detailed next.

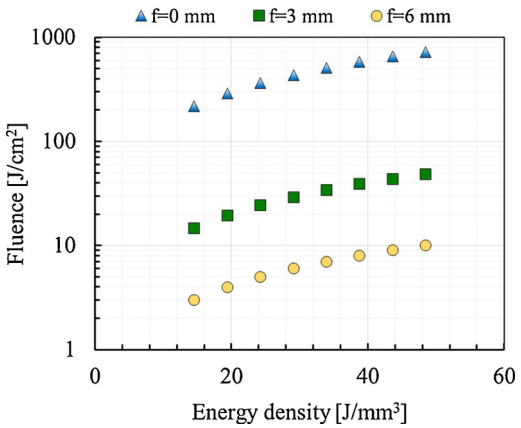

Fig. 1. Relationship between energy density and fluence values tested in the experimental runs.

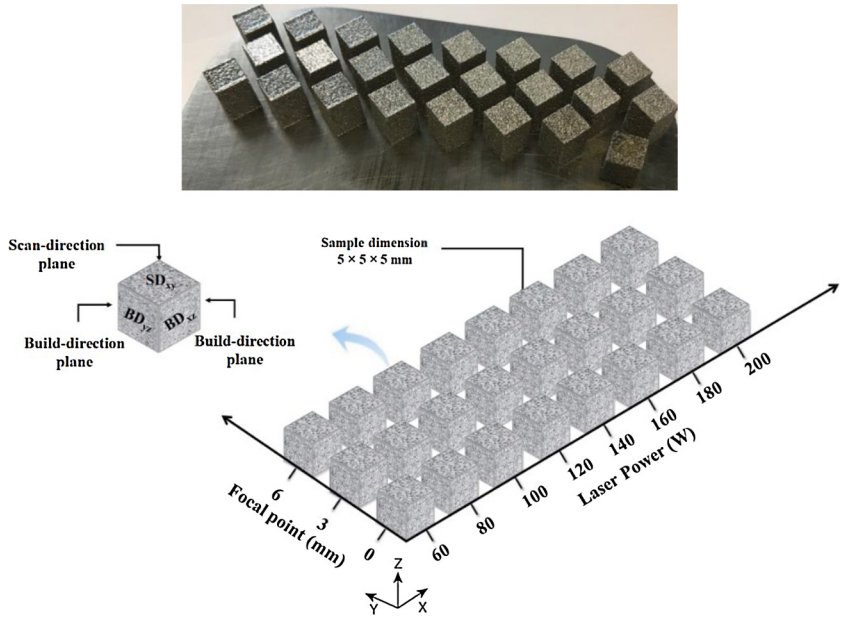

Fig. 2. Layout of array of porous samples, an image (top) and a schematic view (bottom), with a focal point of the laser 0, 3 or 6 mm below the surface of the powder bed. Sample size is 5 × 5x5mm^3.

4.1. Material

Commercially available gas-atomized metal powder CL 20ES Stainless steel (similar to 316 L) [45] was used to fabricate the porous structures. The specification and actual composition (as supplied) are shown in Table 3. The powder morphology was analysed using SEM, shown in Fig. 3.

4.2. Pore size and porosity

Porosity plays an important role in enhancing the transport of fluid and heat through porous structures. There is a wide range of methods for direct imaging to quantify porosity [46]. These include optical light microscopy and SEM. In this paper, the pore size and porosity of porous structures were obtained by two microscopic imaging techniques:

(i) SEM (JEOL JSM-6400) was used to quantify porosity and pore sizes of as-fabricated porous structures. Image analysis evaluates the porosity by computing the pore area percentage on SD (scan direction) and BD (build direction) views of a sample. Several cross-section images were collected and transformed into binary images using ImageJ as image analysis tool.

(ii) A digital microscope (Keyence VHX-5000) was used to capture optical micrographs of polished samples, which allows stitching of multiple images to provide large images of each surface. SD-plane view of 8 samples (f = 0 mm), and BD-plane view of 8 samples (f = 6 mm) were analysed. The porosity and pore sizes of the specimens were quantified by employing ImageJ analysis.

In addition to microscopic image analyses, the porosity of each test sample was measured by two techniques:

(I) the Archimedes method was used to estimate porosity. The sample's weight was recorded independently three times in air and in both ethanol and methanol using a high-precision Mettler Toledo balance (resolution of 0.0001 g) equipped with an immersion density kit. From this, the mass density of the porous sample was estimated by:

$$\rho = \frac{m_d}{m_d - m_w}(\rho_l - \rho_a) + \rho_a \tag{6}$$

where, input data consists of dry mass m_d in air, wet mass m_w, when submerged in a liquid, air mass density ρ_a and liquid mass density ρ_l. The porosity ε in % is determined, by assuming ρ_s as a bulk CL 20ES stainless steel with an apparent density of 8.03 g/cm^3 through:

$$\varepsilon = \left[1 - \left(\frac{\rho_a}{\rho_s}\right)\right] \times 100 \tag{7}$$

(II) direct mass measurement, so-called volumetric mass porosity, was also used for characterizing sample porosity. In this method, the porosity of the specimen (ε) was calculated by dividing the actual mass obtained from dry weighing (m_d), by the volume (V) of the parts obtained from measurements of dimensions and by the bulk density (ρ_s) of CL 20ES stainless steel.

$$\varepsilon = 1 - \frac{m_d}{\rho_s V} \tag{8}$$

4.3. Thermal and fluid properties

4.3.1. Effective thermal conductivity

Several methods have been used to determine the thermal conductivity of complex materials [47,48]. Those include the techniques of transient plane and line source, laser flash and steady state [49–51]. Laser flash and transient source techniques quantify thermal diffusivity and require additional measurements to quantify thermal capacity and determine thermal conductivity accordingly [39,52,53]. The principle

Table 3
Chemical composition of CL 20ES powder (wt%).

	Fe	C	Cr	Ni	Mo	Mn	Si	P	S
CL 20ES	Bal.	0–0.03	16.5–18.5	10–14	2.0–3.0	0–2.0	0–1.0	0–0.045	0–0.03

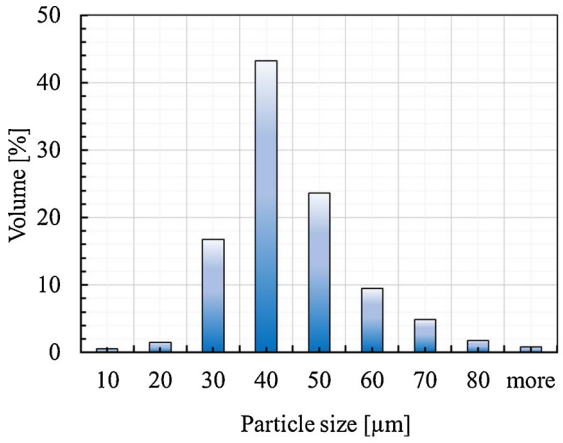

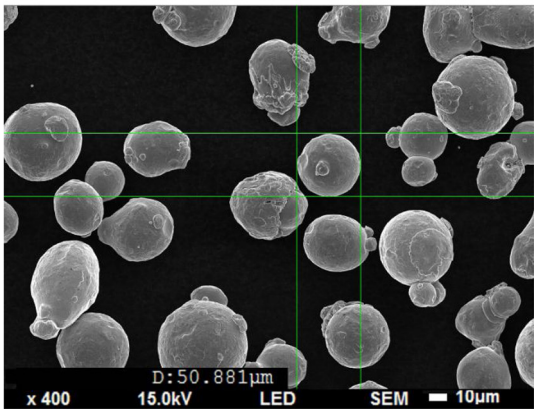

Fig. 3. Powder size and morphology distribution. The particle sizes are sorted by size into 10 μm intervals to quantify the size distribution.

of a steady-state approach is to measure the difference in temperature across the length of the sample, from which the rate of heat transfer is obtained. The main advantages of this approach are the simplicity of the assessment process, good accuracy and precision, and the possibility of unidirectional measurements [34]. Consequently, the steady-state approach was used in this study, permitting the application of Fourier's law of heat conduction.

In Fig. 4, a schematic of the experimental system is shown. The test facility consisted of a system for cooling and heating, a position adjustment system, a system for data collection, and thermal insulation. The porous specimen was placed in series between aluminium blocks above and below the sample. Heat input from the top was provided and heat from the bottom was extracted. The blocks of aluminium act as heat flux meters. The aluminium block contact surface was equal to the sample contact surface, namely $5 \times 5\,mm^2$. The heating system consisted of an aluminium block and 300 W cartridge heater (the upper aluminium block). The lower aluminium block, connected to a cooling jacket with flowing temperature-controlled water, was the lower heat flux meter. By water recirculation, operated by a thermostatic bath, the cooling system was held at a specified temperature.

Three holes in the center of the aluminium heating and cooling blocks are drilled at intervals of 10 mm along the length of both heating and cooling blocks. Six T-type thermocouples of 1 mm diameter stainless steel (three in the upper flux meter and three in lower one) connected to a data acquisition system were used to record flux meter temperatures. The contact conditions between the test sample and heating and cooling blocks were changed by four screws, connecting the top and bottom aluminium blocks. In order to minimize heat losses, all parts of the rig were insulated with Superwool® fibre insulation material. The fluid inside the tested porous structures was still-standing air.

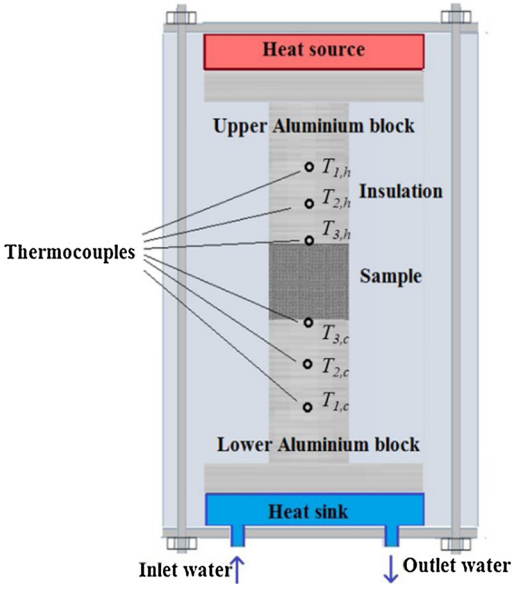

Fig. 4. Schematic view of thermal conductivity measurement setup.

Estimating the ETC value involves three parameters: the heat flux, q; the difference in temperature across the sample, ΔT; and the sample geometry. With these three parameters, the ETC of additively manufactured porous structures can be estimated following Fourier's law of heat conduction. The heat flux is defined as an average of both heat flux meters:

$$q = \frac{k_{Al}}{2}\left(\frac{T_{3,c} - T_{1,c}}{x_{3,c} - x_{1,c}} + \frac{T_{3,h} - T_{1,h}}{x_{3,h} - x_{1,h}}\right) \tag{9}$$

where, k_{Al} reflects the bulk aluminum thermal conductivity, q is the 1D axial heat flux, and $T_{3,c}$, $T_{1,c}$ and $T_{3,h}$, $T_{1,h}$ are the aluminium heating and cooling temperatures, with thermocouple positions given by $x_{3,c}$, $x_{1,c}$ and $x_{3,h}$, $x_{1,h}$, respectively. ETC can be determined using Fourier's law and the well-known concept of thermal resistance from:

$$ETC = \frac{l \bullet q}{\Delta T \bullet A} \tag{10}$$

Where A is the geometric cross-sectional area of the sample, l is the sample length and ΔT is the temperature difference measured across the sample.

By rotating the specimen, each experiment was repeated, measuring the ETC in the three principle directions across the sample, so-called: BD_{xz}-plane, BD_{yz}-plane and SD_{xy}-plane (see Fig. 2). All cross-sectional views as well as average value of all directions of each sample are reported. An aluminium solid block with known characteristics was also tested to calibrate the measurements. It was found that thermal conductivity was within 5% of the solid block's reported value. The uncertainties of parameters which were used in the evaluation of ETC were also evaluated. The uncertainty of the ETC was less than 6.25 %.

4.3.2. Wettability

In the literature, several methods are suggested for determining the contact angle between powder particles or porous structures and a fluid. These approaches include sessile drop and capillary rise methods [54]. The sessile drop based approach is widely used for porous structures [55]. Thus, a facility is designed to measure a liquid droplet's dynamic contact angle on porous surfaces based on a transient measurement of droplet penetration into porous structures.

A syringe pump was used to dispense a single droplet of a known volume at a known frequency. Through a stainless steel needle (50 μl Hamilton syringe) connected to a Rame-Hart Automated Dispensing Device, a droplet was released onto the surface of the additively

Table 4
Physical properties of the ethanol liquid used including impact conditions.

	Properties at 23.5 °C			Impact conditions		
Droplet liquid	ρ (kg/m)	μ (mPas)	σ (N/m)	Volume (μl)	D (mm)	V (m/s)
Ethanol	785.51	1.087	0.0217	4.5	1.9	0.11

manufactured porous structures. A droplet volume of 4.5 μl was used to keep a low Weber number. Simultaneously, the process of droplet impact and penetration through the porous structure was captured using a high-speed camera. All components are aligned with adjustable micrometre stages (light source, camera needle and test stage).

Experiments were carried out to determine liquid-solid contact angles for various additively manufactured porous structures. For each sample the drop impact test was repeated three times on both BD-plane and SD-plane surfaces. Images captured from the high-speed camera are analysed with an image analysis tool for determination of the dynamic contact angle. All experiments are carried out in an air-conditioned laboratory environment at 23.5 °C ambient temperature. Table 4 lists the fluid used in this analysis, ethanol, along with its physical properties.

To quantify the fluid transport aspects of the processed samples, the drop was released from just above the surface (h = 0.96 mm). Placing ethanol droplets on porous surfaces shows three different regimes (see Fig. 5) [56]:

(i) Increasing drawing area (IDA): at first, the droplet extends across the surface (gradually increasing the droplet diameter) and the contact angle decreases slowly until an advancing contact angle, θ_a, is reached and the wetting front stops.
(ii) Constant drawing area (CDA): the contact line remains fixed as the contact angle decreases until the static receding contact angle, θ_r, is reached.
(iii) Decreasing drawing area (DDA): the contact angle remains fixed at θ_r where the contact line decreases until the droplet is fully absorbed in the surface and disappears.

These dynamic angles (see Fig. 5) are used to estimate the equilibrium contact angle or so-called contact angle hysteresis, θ, which is defined by the measured advancing and receding contact angles ($\theta = \theta_a - \theta_r$) [57,58]. The determined equilibrium contact angle is used in Eq. (1) and $r_{eff} = r_p \cos^{-1}\theta$ to compute the capillary pressure and effective pore radius in this study.

5. Results

In this section the experimental characterization results of the SLM-fabricated samples are presented. In Section 5.1 the morphology is investigated using SEM for as-fabricated samples and optical microscopic for polished samples. The pore size distribution is discussed in Section 5.2, while the porosity/mass density results are collected in Section 5.3. Thermal conductivity is addressed in Section 5.4 and the wettability of the printed samples is considered in Section 5.5.

5.1. Scan direction (SD) and build direction (BD) surface morphology

The porosity and pore sizes of the fabricated samples are associated with melt flow behaviour. The precise details depend on laser process parameters, resulting in a wide variety of melt flow traces that are discussed in this subsection. Typical solidified SD-plane and BD-plane surfaces of as-fabricated samples (f = 0 mm) from SEM imaging are shown in Fig. 6. The images correspond to combinations of parameters listed in Table 2. The scanning direction is also indicated in the figures by the green arrows. When laser power is applied to the powder bed, the powder particles form a melt pool. Based on the laser power applied, the porous structures show a distinct difference in melt track morphologies. Different regimes are discussed next:

- 200 W: from the cross-sectional views, the laser scan tracks appear uniformly lined up at a laser power of 200 W and tracks frequently overlap with neighbouring tracks.
- 180 W: the tracks become somewhat irregular at 180 W and at some locations open pores occur
- < 140 W: for laser power less than 140 W, insufficient energy is applied to fully melt all powder particles; therefore, hatch lines no longer form continuously. This is associated with the formation of a porous structure. By further decreasing laser power, the melt pool size is gradually reduced and since hatch spacing remains constant, this results in the reduced overlap and further increase of the porosity. Severe voiding occurs at power levels below 140 W and many pores are produced. The pores are randomly distributed along and between the hatch lines with irregular morphology.

During the printing process, melt pool accumulation was observed and as a result of surface tension rounded surfaces are formed, as long as the melt pool does not wet the previous layer or adjacent hatch line. This effect is commonly known as balling [16] and is a defect formation mechanism in SLM, which generates lack-of-fusion porosity typically due to low energy density. Sintered powder particles are mostly visible in the side cross sections (BD-plane) and occur at all power levels.

Fig. 7 shows representative polished sample areas used for pore size and porosity assessments at different laser powers (60 W to 200 W) and focal positions (f = 0 mm and 6 mm). It is obvious that the pore characteristics are highly dependent on laser power – larger pores are irregularly formed at lower laser powers in all samples. As the laser

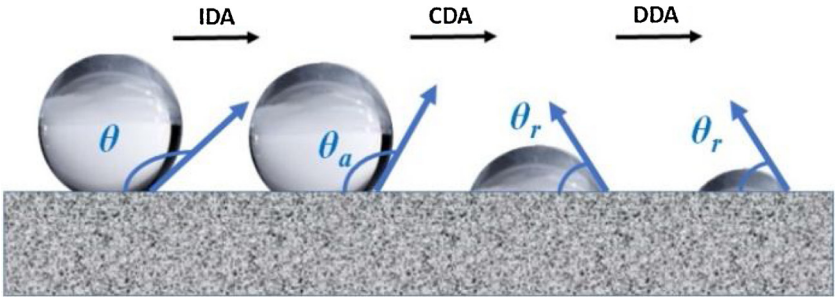

Fig. 5. Different contact angles on the porous surface: advancing contact angle, θ_a, and receding contact angle, θ_r, as well as different regimes for droplet infiltration into a porous structure: increasing drawing area (IDA), constant drawing area (CDA), and decreasing drawing area (DDA).

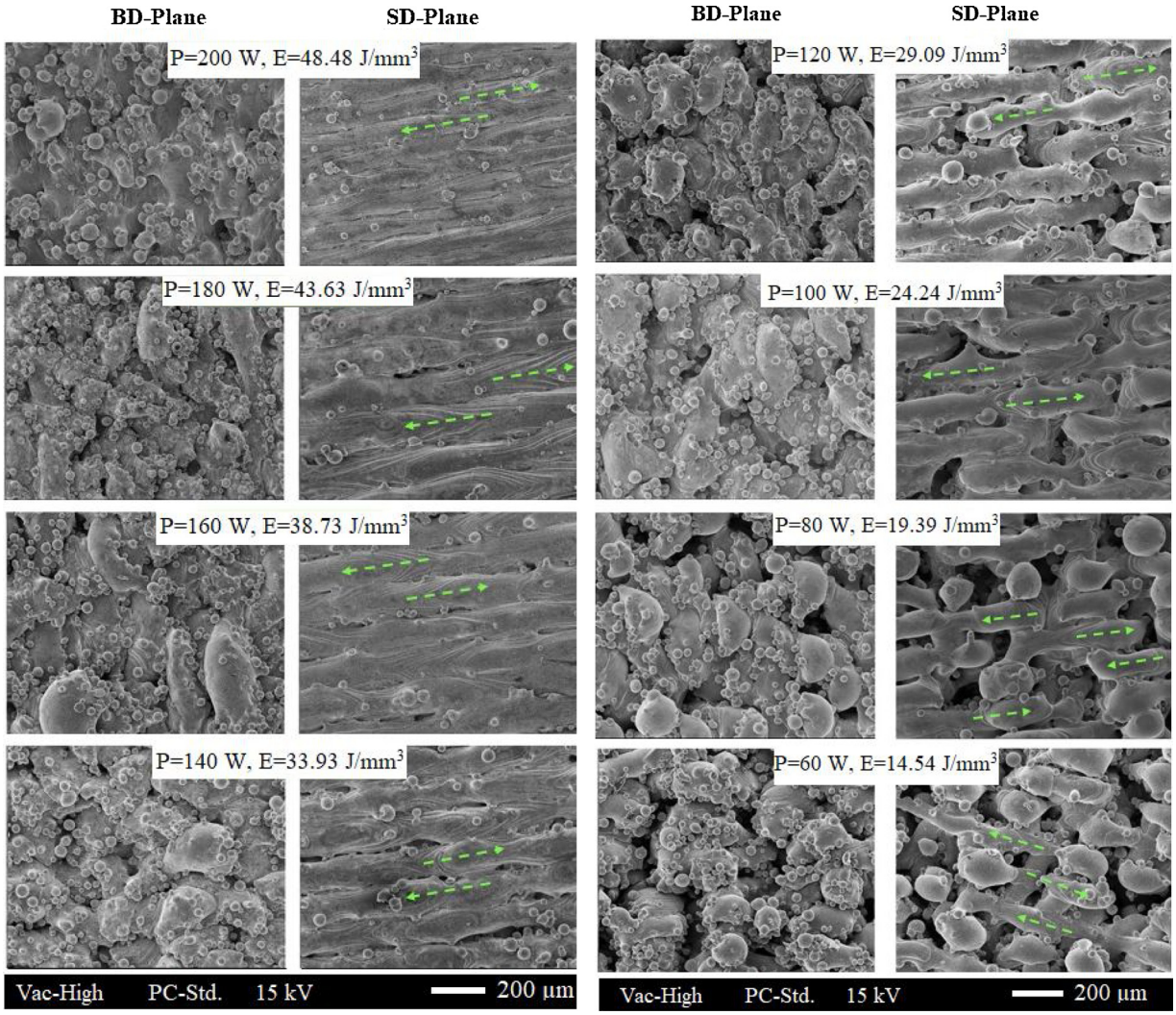

Fig. 6. SEM images of BD-plane view and SD-plane view of laser molten structures (f = 0 mm) following the experimental design of Table 2. Green arrows indicate the scan direction. BD designates the build direction, while SD designates scan direction.

power increases, the pore size gradually decreases and the interconnectivity of the pores becomes lower. In the end, as shown in both BD-plane and SD-plane views, most pores close at a laser power of 200 W. This is consistent with the analysis from Fig. 6 for as-fabricated SEM image analysis discussed above.

5.2. Pore size

A porous structure's pore size is a primary determinant of its function as discussed in Section 2. Therefore, Fig. 8 displays the effect of laser power and focal position on BD-plane and SD-plane pore sizes of as-fabricated samples. Average pore sizes of structures observed in the BD-plane at laser powers of 180 W and 200 W are larger than those seen in the SD-plane. When laser power is high, molten metal has time to fill the open spaces between powder particles within the powder bed, causing the pores to drop in size and almost form a continuum – this process is more effective in SD-planes. As laser power is decreased from 140 to 80 W, average pore sizes increase slightly while a rapid rise in pore sizes (14–25%) is observed from 80 to 60 W in both side and cross sections. When the pore size of porous structures is significant, this threshold should be considered. It was also found that focal position does not affect the pore size significantly.

Fig. 9 presents the pore size distribution results for the SD-plane (f = 0 mm) according to SEM image analyses of as-fabricated samples and digital image analysis of polished samples. The pores are sorted by size into 10 µm intervals to produce size distribution plots. Note that for each section the total area analysed is much greater than the representative sections shown in Figs. 6 and 7. The distributions confirm that polished samples have a much higher frequency of small pore sizes compared to original as-fabricated samples. This is because pores are disrupted during polishing. A similar peak in both polished and as-fabricated samples is observed; however, the peaks shift from 20 µm for a laser power of 200 W to 40 µm for a laser power of 60 W.

5.3. Porosity/mass density

Fig. 10 indicates the variation in mass density within the porous samples determined by the Archimedes method as a function of laser power and adopted focal point. Concerning the Archimedes method, different fluids (ethanol and methanol) were utilized. It appears that both fluids yield the same measurement of mass density. This is because of very similar surface tensions of the selected fluids (~22 N/m at 20 °C). This low surface tension affects the ability of the fluid to correctly wet the entire surface of the samples. The porous mass density varies between 4.63 and 7.83 g/cm^3. As shown in the figure, three zones can be observed: the mass density is quite independent of laser power near the highest and lowest energy densities adopted, while a rapidly increasing mass density is observed for laser powers above 80 W,

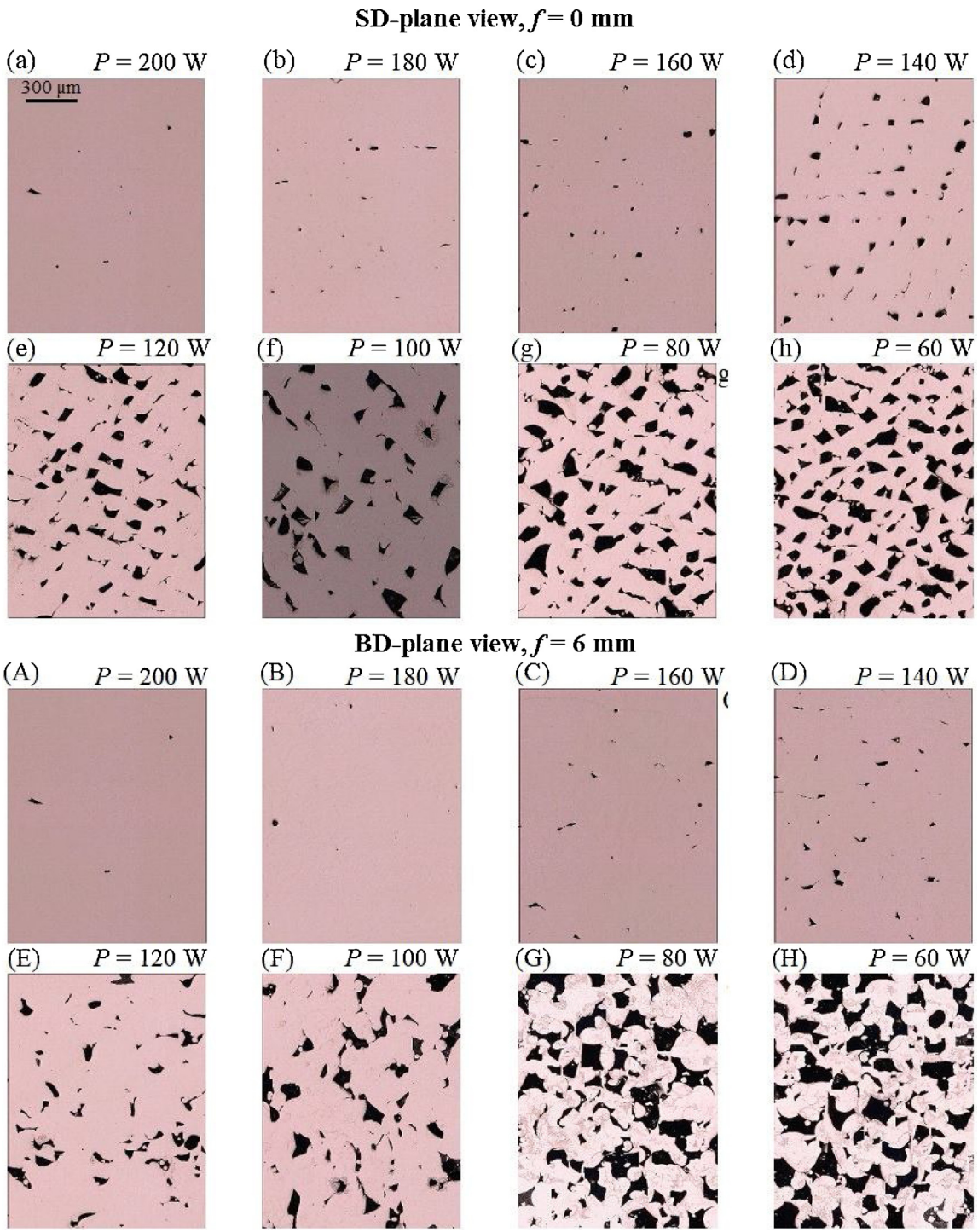

Fig. 7. Optical microscopic of polished samples, showing porosity in (a-h) SD-plane view, f = 0 mm and P = 200, 180, 160, 140, 120, 100, 80 and 60 W (A-H) BD-plane view, f = 6 mm and P = 200, 180, 160, 140, 120, 100, 80 and 60 W. Black areas identify open structures in the section of the porous sample.

saturating for laser powers about 160 W. At lower energy densities, i.e., for highly porous structures, the focal position has a marked influence. Reducing f, i.e., reducing the laser spot size and, thus increasing the fluence of the laser radiation, results in a higher mass density sample being produced. These results are consistent with the cross-sectional morphology of porous structures.

The porosity measurement results using different methods including the volumetric and Archimedes porosity measurement methods, and image analysis of as-fabricated samples (SEM) and polished samples (optical microscopy) were obtained. Fig. 11 shows the relation between porosity as determined by Archimedes method compared to other methods. On the basis of Fig. 11:

5.3.1. Archimedes method vs volumetric mass density method

As evidenced in Fig. 11, porosity decreases with an increase in laser power. At a laser power of 60 W, the total porosity determined by volumetric mass density test is 31 %, 36 % and 44 % for a focal point of f = 0, 3 and 6 mm, respectively. The open porosity determined by the Archimedes method is 30 %, 34 %, and 42 %. Note that the volumetric porosity measurement to obtain total porosity was performed by

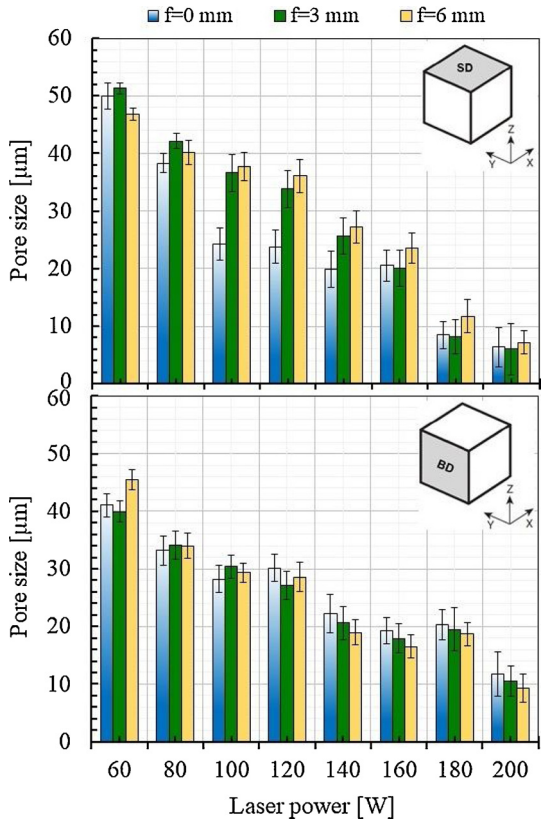

Fig. 8. Average pore sizes for SD-plane (top) and BD-plane (bottom) as a function of the laser energy power and focal point.

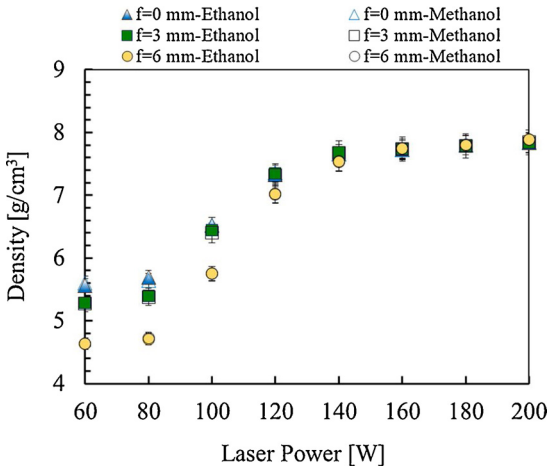

Fig. 10. Dependence of porous structure mass density as a function of the energy power.

measuring the outer physical dimensions. The weight of the porous structures and bulk mass/volume ratios were determined before the Archimedes test was performed. Hence, the pores did not contain any fluid at this stage. Since the Archimedes method gave approximately the same results as the volumetric method, the number of pores accessible to the measurement liquid is similar to the total number of pores. Hence, most of the porosity is interconnected. Moreover, microscopic (polished) samples showed that pores are interconnected (see Fig. 7) and porosity measurements of as-fabricated samples showed that there are open pores on the surface as well. It should be noted that the high surface roughness of the additively manufactured porous

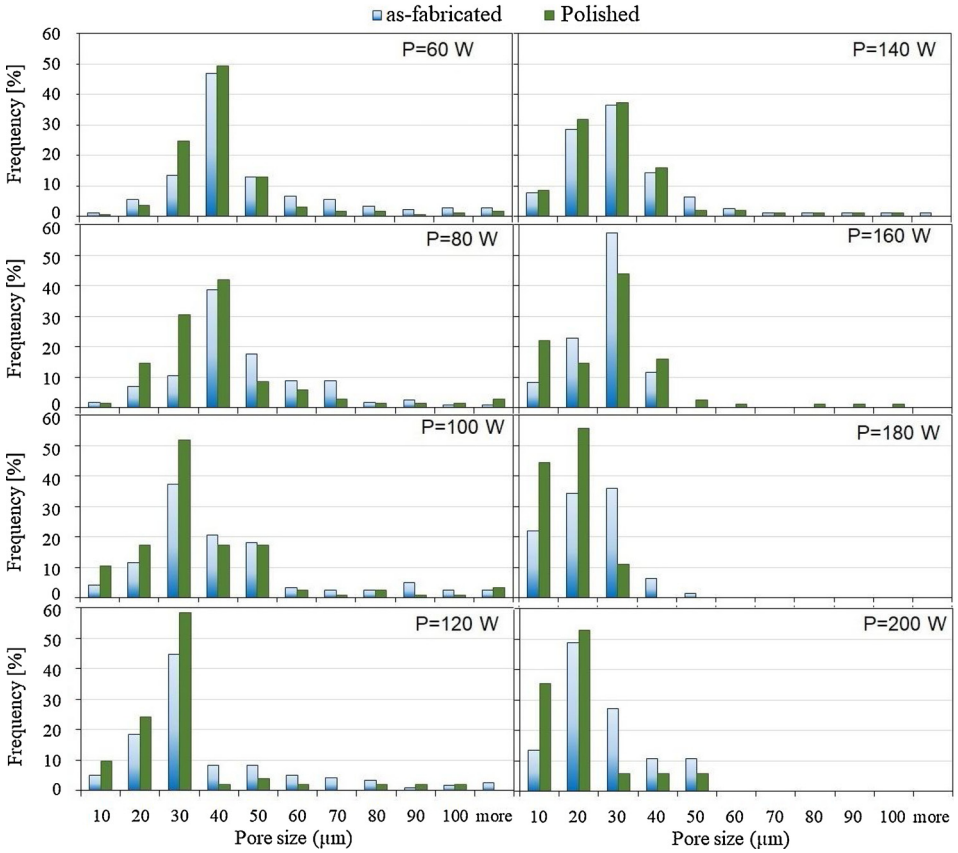

Fig. 9. Pore size distribution comparison of as-fabricated samples via SEM and polished samples via optical microscopy, showing relative frequency of pores for f = 0 mm and laser power of 60-200 W.

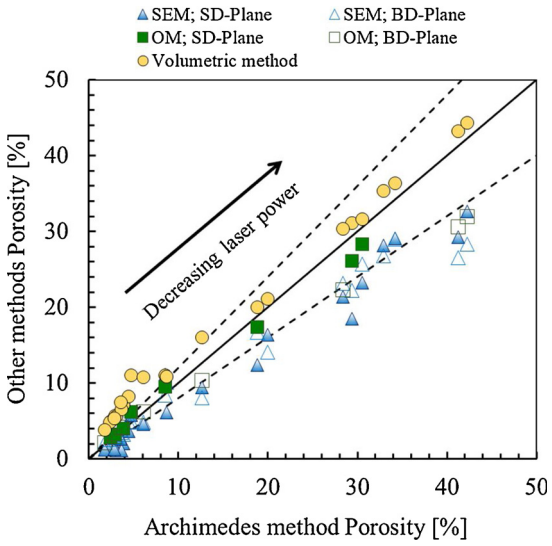

Fig. 11. Comparison of porosity measurements. The solid line shows equivalence between Archimedes method and other test methods: SEM, OM (optical microscopy) and volumetric mass density. Dotted lines show a deviation of 20 % from the equivalent behaviour.

structures (see Fig. 6) may lead to the formation of some residual air trapped inside the porous structure. These findings are in agreement with results of [59–62].

5.3.2. Archimedes method vs image analysis

The polished and as-fabricated porosity values are very similar and close to those determined by the Archimedes process, except at low laser power. For samples with higher porosity, the measurement of porosity using image analysis methods is lower than using the Archimedes method. A disparity between the results of the Archimedes method and the image analysis method may occur because image analysis may include the effect of unmolten powder on the porosity values, since the cavities may contain unmolten powder.

It appears that the Archimedes approach determines more reliable results as the entire volume of the specimen (in 3D) is considered rather than the upper/side surfaces (in 2D), which may not reflect an accurate average porosity of the sample. Hence, the findings of the porosity measurement based on the Archimedes test are considered for the following discussion.

5.4. Thermal conductivity

The ETC relies on both the properties of solid and liquid material as well as the composition of the porous matrix, which is defined, e.g., by its distribution of porosity and pore volume. It is recognized that the thermal properties of porous structures, in particular, the thermal conductivity, are significantly different from those of the corresponding solid bulk material. The morphology of porous structures, as evidenced in Fig. 12, may affect the macroscopic transport properties, i.e., the thermal conductivity. The thermal conductivity along three principle orientations is measured in order to gain directional dependence of the thermal properties of the porous structures. Hence, it is possible to detect isotropic properties of porous structures. The measured thermal conductivity for the *xz*-build direction plane (BD_{xz}) versus scan direction plane (SD_{xy}) as well as the *yz*-build direction plane (BD_{yz}) versus scan direction plane are shown in Fig. 12. The data indicates that:

(a) at high porosities (low laser powers) the thermal conductivity of BD planes (k_{BD}) corresponds to the thermal conductivity of the SC plane (k_{SD}) – At higher porosities, the pores and the interconnected networks are, on average, relatively similar, and transport proceeds within the sintered/partially molten material. Consequently, $k_{BD} \simeq k_{SC}$. Moreover, since there are huge numbers of interfaces in additively manufactured porous materials due to the high interfacial thermal conductivity among the connected particles, multiscale feature sizes and multi-dimensional pore sizes can result in similar thermal properties at higher porosities. Hence, the anisotropy in the structure of the materials (see morphology in Fig. 6) does not cause a significant change of the heat conductivity with a variation of the orientation at higher porosities (lower thermal conductivities).

(b) at lower porosities (high laser powers): $k_{BD} > k_{SC}$ – Heat is carried through the BD-planes by molten or partially sintered particles parallel to the direction of the laser scanning. Hence, directional-dependent thermal transport in samples with higher laser powers (lower porosities) can be explained by the inter-layer based on the thermal contact resistance. Based on Fig. 6, the morphological variation may be another reasonable explanation for the variation in thermal conductivity.

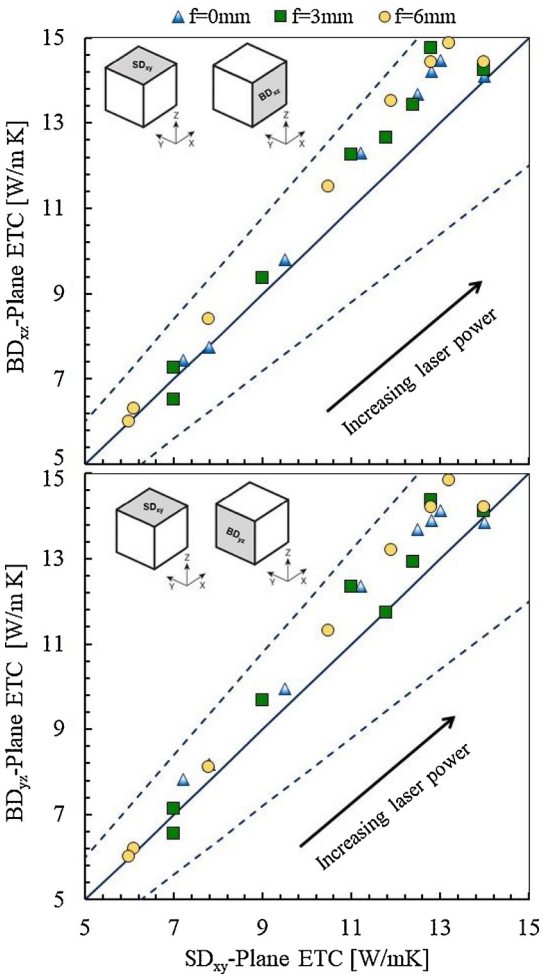

Fig. 12. Comparison of effective thermal conductivity (ETC) measurements. The solid line shows equivalence between test directions: scan direction (SD_{xy}) vs. build direction (BD_{xz}) (top) and BD_{yz} (bottom) i.e. perfectly isotropic behaviour and dotted lines show a deviation of 20 % from isotropic behaviour.

The effect of porosity on the average measured ETC of porous structures relative to the thermal conductivity of the solid bulk material is shown in Fig. 13. This includes predicted curves from various correlations and models presented in Table 1. The pore size, porosity and corresponding ETC are also summarized in Table 5. The primary heat

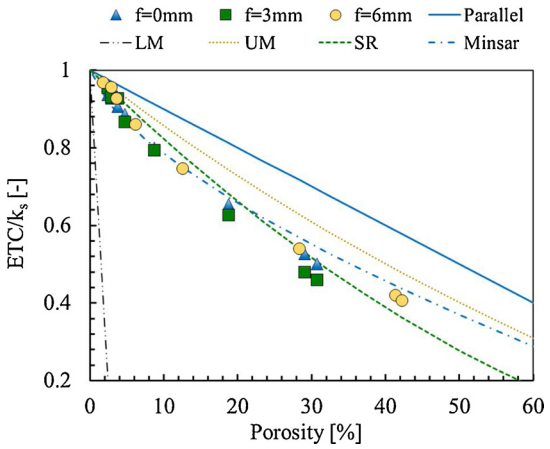

Fig. 13. Comparison of the ETC predicted through the models and correlations: Parallel model, Upper Maxwell (UM) model, Lower Maxwell (LM) model, scaling relation (SR) model and simplified series-parallel and the Misnar model (Minsar) (see Table 1) and experimental data in the current study, as function of the porosity.

Table 5
Laser parameters, geometrical parameters and experimental results of effective thermal conductivity and wettability of additively manufactured porous structures, where f is the focal position, E is the energy density, θ_a is the advancing contact angle, θ_r is the receding contact angle, ε is the porosity, ETC is the effective thermal conductivity, P_c is the capillary pressure, r_{eff} is the effective pore radius and K is the permeability.

f (mm)	E (J/mm^3)	θ_a (°)	θ_r (°)	ε (%)	ETC (W/m^2 K)	P_c (kPa)	r_{eff} (μm)	K (μm^2)
	48.4	31.33	16.75	2.4	14.05	14.8	9.3	0.001
	43.6	32.06	17	2.9	13.9	13.9	9.9	0.003
	38.7	30.8	17.18	3.8	13.6	10.2	13.0	0.010
0	33.8	32	18.09	4.7	13.29	9.6	14.4	0.018
	33.9	33.96	14.5	8.7	12	9.4	14.3	0.062
	24.2	40.1	13.34	18.7	9.8	7.1	17.8	0.512
	19.4	45.53	11.36	29.1	7.9	5.2	22.8	2.288
	14.5	47.07	11.04	30.7	7.5	4.1	28.1	3.866
	48.4	32.5	15.81	2.3	14.32	15.9	8.6	0.001
	43.6	32.5	16.35	3.1	13.95	14.3	9.6	0.003
	38.7	34.05	17.04	3.6	13.9	10.4	13.2	0.008
3	33.8	35.85	17.05	4.3	13	8.3	16.2	0.018
	33.9	31.46	15.77	8.4	11.9	8.7	15.8	0.074
	24.2	33.87	13.36	19.9	9.4	7.5	17.8	0.660
	19.3	39.6	11.19	32.7	7.2	5.8	21.6	3.274
	14.5	41.08	10.92	34.1	6.9	4.7	26.3	5.307
	48.4	32.38	16.16	1.9	14.52	16.0	8.5	0.001
	43.6	31.06	17.88	2.9	14.35	13.4	10.3	0.003
6	38.7	31.5	17.18	3.5	13.92	10.1	13.7	0.008
	33.8	32.96	17.49	6.1	12.9	8.6	15.9	0.038
	33.9	34.1	14.45	12.5	11.2	7.8	17.1	0.203
	24.2	39.1	13.7	28.3	8.1	7.0	18.5	1.665
	19.3	45.51	10.3	39.3	6.3	5.1	22.6	5.483
	14.5	45.78	9.51	42.2	6.1	4.0	28.6	10.832

transfer mechanism is conduction through the metal network ligaments. For all curves, the trends with respect to porosity are similar. Heat conductivity is found to be sensitive to porosity in additively manufactured porous structures. It increases as the porosity decreases. This is due to the fact that heat transfer through still-standing air and sintered/partially molten particles is considerably lower than through the solid material. Reducing porosity increases the thickness of the struts, leading to higher ETC values. Lima et al. [63] also measured the properties of samples produced using conventional metal sintering of stainless steel 316 L. Instead of a gradual reduction in thermal conductivity as porosity increased, evidenced by results found in this paper and also in additively manufactured stainless steel 316 L by [64], a large drop in thermal conductivity at about 8% porosity was observed. Hence, porosity is not the only factor contributing to the reduction in thermal conductivity. It also depends on the morphology and surface roughness of materials.

There is a strong correlation between porosity and thermal conductivity. It can be seen that over the range of input energies the relative density changes by ~28 %, ~32 %, and ~41 % (for f = 0 mm, f = 3 mm and f = 6 mm, respectively), while the ETC changes by 45 %, 51 %, and 57 %. This implies that the thermal conductivity is not only influenced by the densification of the sintered particles, but also affected by changes to the morphology. In particular, the connectivity between the powder particles increases with increasing focal distance (f) as well as laser power (Fig. 6) by two mechanisms, sintering and localised-partial melting.

These results show that, like structural properties discussed in Sections 4.1–4.3, thermal properties are also affected by SLM process parameters. If the laser power of the process is too low, the thermal conductivity is reduced more than predicted by effective medium models (dependence of thermal conductivity on the porosity alone). As evidenced in Table 5, the experimental results showed thermal conductivity increased by around 45–57% (depending focal point) as laser power increases from 60 W to 200 W.

Experimental data for thermal conductivity, compared with models presented in Table 1 indicate that:

The parallel model and Upper Maxwell theory represent an upper limit and the lower Maxwell theory represents a lower limit for the thermal conductivity trend as expected.

- Lower Maxwell theory is suitable for materials where the continuous phase's thermal conductivity is higher than the dispersed phase's thermal conductivity, such as foam or sponge materials
- The Parallel model assumes the phases are parallel to the heat flow, thus having alternating parallel conduction paths. While this model is not physically correct for our samples, this model gives an upper bound for the thermal conductivity.

Experimental data falls between the Upper Maxwell model, scaling relation model and the Misnar model with a porosity value of less than 10 %.

- The Upper Maxwell model over-predicts the thermal conductivity by approximately 20 %. The error can be contributed to changes in the (micro)structural and surface properties due to the AM process. Maxwell's theory is also known for the prediction of spherical pore thermal conductivity. Hence, these effective medium models can not accurately reveal the influence of the porous network morphology, surface roughness and pore size distribution on the effective thermal properties of additively manufactured porous structures.
- The experimental data was confronted with a simplified series-parallel model and the Misnar model with a total discrepancy of less than 10 %. This model applies to open-cell porous structures, taking into consideration both the solid-fluid interface and porosity. However, the model does not consider generated tiny solid-solid interfacial connection structures (necking particles) in additively manufactured porous structures.
- The scaling relation model also predicts experimental results within a 15 % error. This model takes into account the effect of porosity of porous structures and is applicable to sintered metal particles.

In summary, it can be concluded that the ETC decreases as the porosity increases for all tested samples. The effect of pore size on ETC is less important and in our sample collection, there is generally no noticeable effect of pore size. Above discussed models neglect the existence of "necks" linking pores and pore size distribution in actual additively generated porous structures as well as multiscale features, i.e., sintered-like powders. That may contribute to the difference

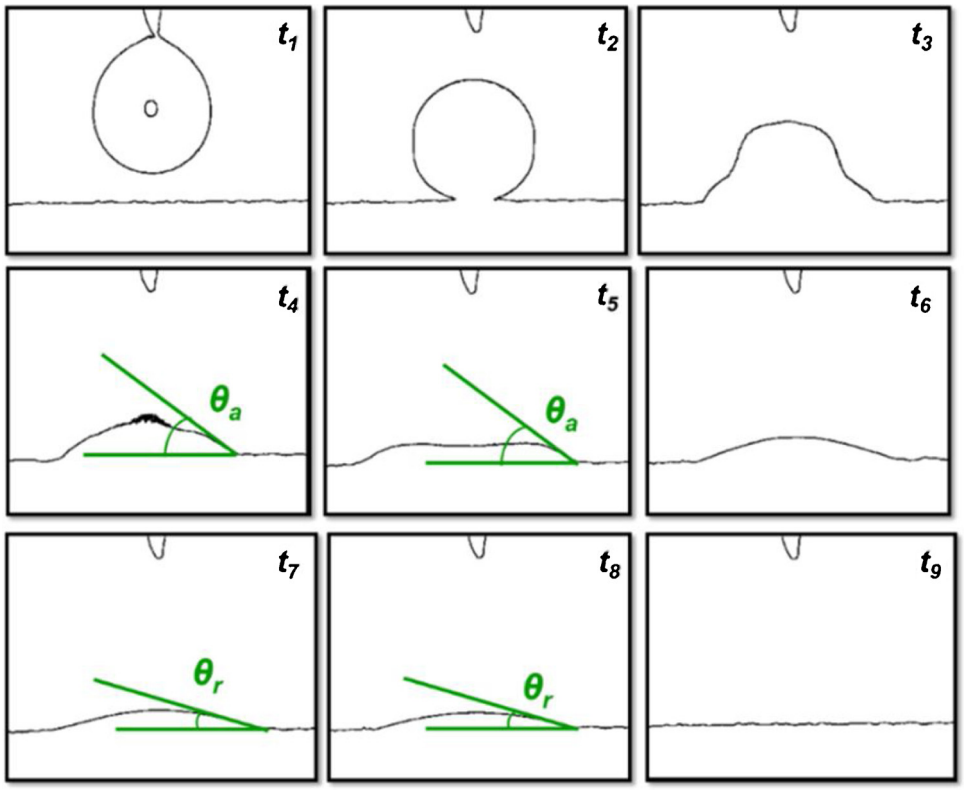

Fig. 14. An example of a droplet falling onto a porous surface.

between experimental data and correlations. On the other hand, it is revealed that porosity alone is not enough to describe the effect of voids on thermal conductivity; other factors such as morphology and void form should also be taken into consideration. In a wide range of porosity, therefore, a single model may not be able to correctly predict all the experimental data. Therefore, for the thermal conductivity of additively manufactured porous structures, we believe it is more reasonable to estimate upper and lower limits. We notice the Upper Maxwell equation providing an upper bound, while the lower bound is not clearly identified since the difference between the experimental data and the lower boundary is high. Further research is needed, taking into account multi-scale interfaces, to establish boundaries for thermal conductivity of additively manufactured porous structures.

5.5. Wettability

In this subsection, the wettability is studied in order to quantify the fluid transport aspects of the additively manufactured specimens. For BD- and SD-planes, we defined and characterized spreading and contact angles. Fig. 14 shows typical examples of the impact process, obtained from high-speed video sequences as a droplet falls onto the surface and infiltrates the porous medium. Fig. 15 shows the resulting transient drawing area and contact angle as a function of time. The figure shows three droplet measurements (f = 0 mm and P = 60 W) on a sample's SD-plane. The plots are segmented into the three droplet penetration stages that are easily identifiable. The spreading diameter initially rises to around 3.8 mm after the droplet is released onto the surface. At the end of the IDA stage the contact angle of 47° is taken as the advancing contact angle, θ_a (see also Fig. 14, t_4 and t_5). The contact line remains constant (CDA), and the angle of the contact angle decreases relatively linearly. Subsequently, the contact angle is fixed as the diameter of the droplet decreases (DDA) until it is fully absorbed into the porous structure. During this phase the constant contact angle of ~ 11° is taken as the receding contact angle, θ_r (see Fig. 14, t_7 and t_8).

The wettability of the SD-and BD-planes of the additively manufactured porous structures are reflected by the contact angle. Fig. 16 shows the impact of single ethanol droplets that penetrate into the SD- and BD-planes of samples of different porosity. The advancing

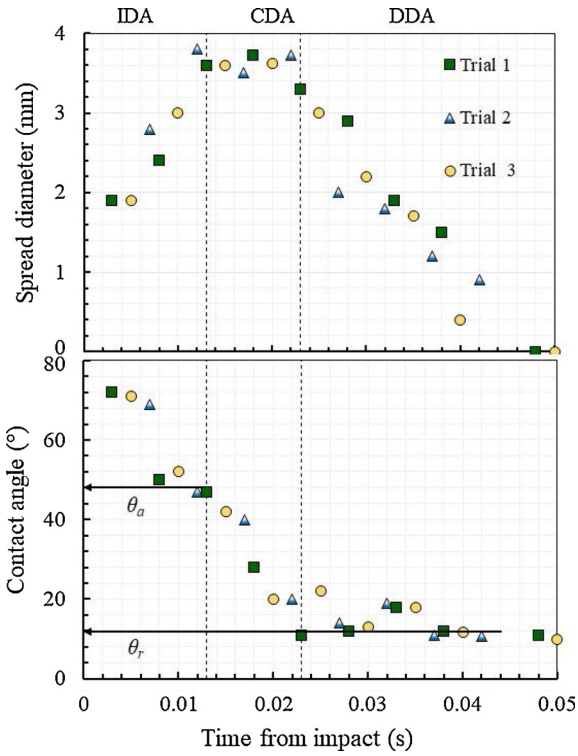

Fig. 15. Plots of the spreading diameter (top), and the contact angle (bottom) as a function of time after droplet impact with the surface (3 trials) for a sample (f = 0 mm and P = 60 W).

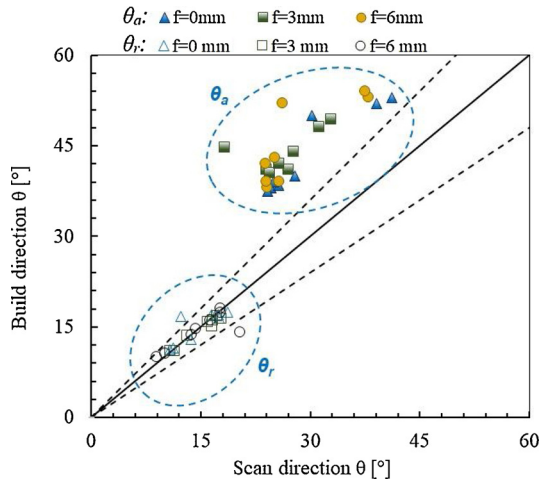

Fig. 16. Relation of advancing contact angle (θ_a) and receding contact angle (θ_r) of BD-and SD-planes. The solid line shows equivalence between test directions (build direction vs. scan direction) and dotted lines show a deviation of 20 % from the isotropic behaviour.

dynamic contact angle (θ_a) and receding contact angle (θ_r) are relatively constant for porosities less than 10 %. As the porosity increases the θ_r value decreases and the θ_a value increases. The advancing contact angle of the SD- and BD-planes of the porous structures showed an increase from ~ 31° to 46° and ~ 38° to 54° with increasing porosity (decreasing the laser power). We have observed the same changes in receding contact angle. Although the surface chemistry on both surfaces is the same, the BD-plane's contact angle of equilibrium is about 18 % greater than the SD-plane.

Porosity and pore size (Fig. 17) were found to affect the contact angle as well. With increasing porosity, the contact angle of porous structures increases. This can be due to the near-zero contact angle in small pores of the fluid [65,66]. With increasing porosity, the pores become larger and the contribution of morphology becomes less. Minimum wetting contact angle for advancing and receding liquid for stainless steel was reported for advancing/receding contact angle as 19°/8° [67]. The additively manufactured porous structures exhibit a larger advancing/receding (30°/16°) contact angle. Since the surface roughness contributes to an increased contact angle, it can be expected that additively manufactured porous structures have a higher equilibrium contact angle.

We have determined that besides the impact of pore size and porosity, the surface properties determine the wettability. Specifically, we observed differences between the BD- and SD-planes for the advancing contact angle. This may be due to the low surface tension of ethanol, which promotes the spread and is less affected by roughness during penetration. This is, in fact, consistent with previous work in which roughness has had a limited effect on low-surface tension droplets that spread over wettable substrates [68,69]. Overall, compared to the effect of porosity and morphology on the receding contact angle, the effect of porosity and morphology on the advancing contact angle is more pronounced.

6. Discussion

In this section, the porous structures and corresponding thermal and fluid flow properties as manufactured with the SLM process under a range of printing conditions will be reviewed and improvements of the capillary performance are discussed. The geometrical, thermal, wettability and hydraulic behaviour of additively fabricated porous structures are summarized in Table 5. The fabrication and characterization of the capillary performance of hydrophilic (14° < contact angle < 36°) SD-plane porous structures with porosity as high as 42 % is reported.

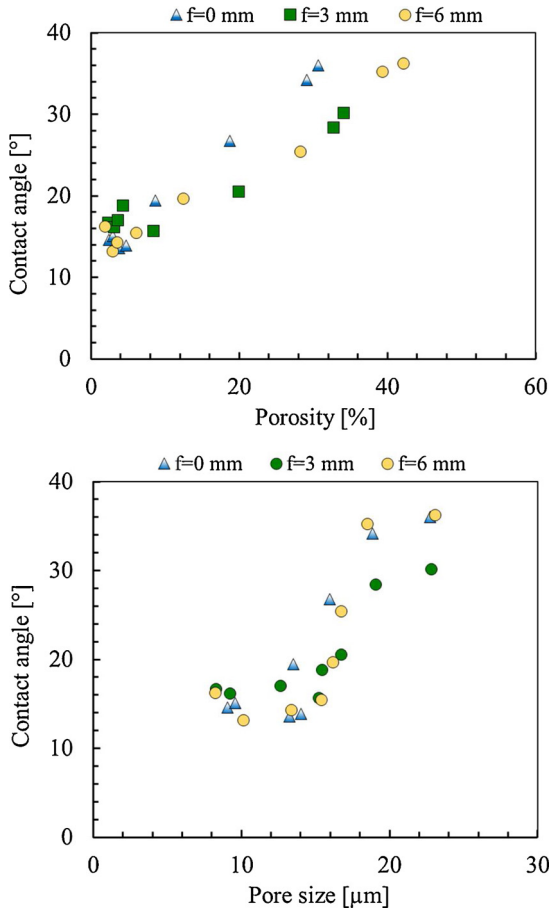

Fig. 17. Relation of equilibrium contact angle (θ) and porosity (top) and pore size (bottom).

The liquid-solid surface contact angle is a crucial parameter used in calculating the capillary pressure supplied by a porous structure. When assessing the overall capillary quality of porous structures, the pore size (r_p) and porosity (ε) are also critical factors. The capillary pressure and effective pore radius are determined from the pore size and contact angle of the measured porous structure. Therefore, the most commonly adopted limiting performance metric for two-phase devices [9,38], the capillary performance parameter K/r_{eff}, is used in this discussion.

According to Eq. (1) the maximum capillary pressure corresponds inversely to the pore radius. The capillary pressure ranges from 4 to 7.5 kPa for the manufactured porous structures with porosity of 18–42 %. A small pore radius leads to high capillary pressure, but in general it also decreases the permeability. It was observed that the permeability changes from 0.6–10 μm^2 for higher porosity samples (18–42 %). Table 5 shows the permeability and capillary pressure values for different values of porosity. The capillary performance parameter K/r_{eff} captures the trade-off between these two competing effects. Since the effective pore radius is less sensitive to porosity, the ratio of K/r_{eff} increases with increasing porosity, as shown in Fig. 18 (only structures with a higher porosity are included in the figure).

The values of K/r_{eff} are plotted versus pore radius in Fig. 18 as well. Clearly, capillary performance is higher for relatively identical pore sizes for samples with a higher porosity (focal positioning at 6 mm). For instance, at a pore size of ~ 22 μm, the porosity ranges from 30 to 42 %, which gives a permeability (K) of 3.8×10^{-12} to 1×10^{-11} m^2 and therefore K/r_{eff} ranges from 0.13 to 0.23 μm. The capillary performance of additively manufactured specimens also improves with increasing pore radius from 16 to 22 μm. This means that using AM, the two competing effects on capillary performance, due to pore size and

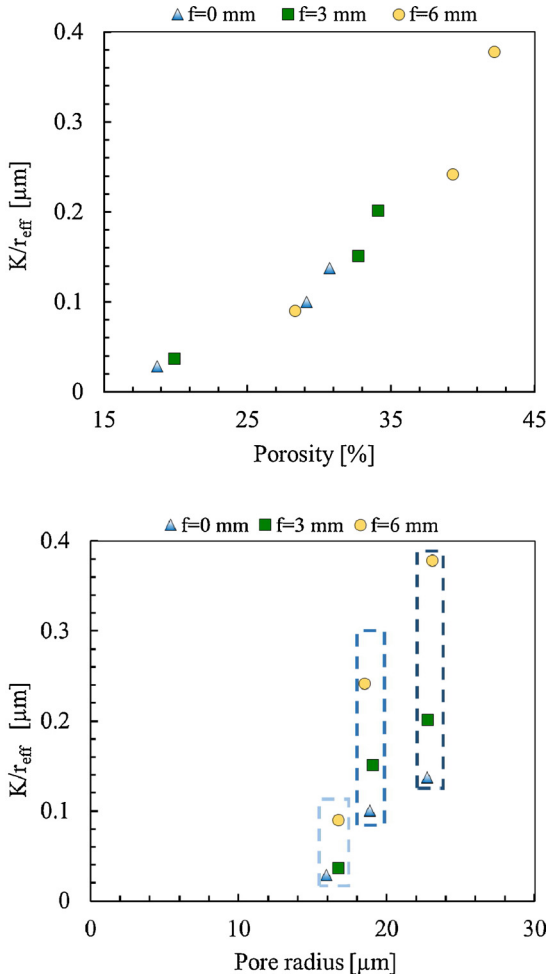

Fig. 18. Relation between the capillary performance parameter (defined as K/r_{eff}) for higher porosity samples (~ 18-42 %) and porosity (up) and pore size (down).

porosity, can be balanced intricately.

It is important to compare the current results with previous literature studies. As discussed, the effective pore radius depends on the fluid used, unlike the permeability (K). The values obtained for K/r_{eff} are therefore also dependent on the liquid of choice. An example in the open literature for sintered stainless steel porous structures with ethanol as test fluid was not found. Therefore, stainless steel metal foams are chosen for comparison (see Table 6). These results show a similar K/r_{eff} for a metal foam with 68 % porosity and an additively manufactured porous structure with 43 % porosity. This demonstrates that additively manufactured porous structures have the potential to push even at lower permeability and porosity beyond the limited transport by regulating pore sizes.

For heat pipe applications, the dependency of the capillary performance measure K/r_{eff} on porosity and pore size can be exploited directly. In fact, using AM, local variations in porous structures can be produced. Realizing smaller pores providing higher capillary force is advantageous for wicking liquid, while realizing larger pores to provide pathways for evaporated vapour. Realizing both structures next to each other allows for optimizing heat pipe performance by tuned transport characteristics. This is a unique advantage of fabricating porous structures additively. The fabrication approach of gradient additively manufactured porous structures offers a new architecture that provides beneficial (wicking) capabilities that can be used to build next-generation thermal management devices and other potential application fields as well.

Table 6
Comparison of capillary performance of additively manufactured porous structures and sintered porous structures.

	Current study		Metal foam [66]		
Porosity, %	~ 36	~ 43	68	75	82
Permeability, µm^2	5.4	10.0	31	59	94
K/r_{eff}, µm	0.24	0.37	0.34	0.56	0.69

7. Conclusions

The main aim of this paper was to investigate the viability of using SLM to additively fabricate metal porous structures. The influence of laser process settings on the porosity and pore sizes of the additively manufactured porous structures was analysed. CL20ES stainless steel powder was used as powder feedstock material. The effects on porosity and pore size were determined, and porous samples were characterized in terms of thermal conductivity, wettability and capillary performance. The main results obtained are as follows:

- It is important to manage the energy density per unit volume as well as the beam size. It was shown that control of energy density using fluence can be highly advantageous. Interconnected micrometric cavities could be obtained along fabricated samples by exploiting the lack of fusion at sufficiently low laser power. Indeed, using a relatively low energy density led to a shift in the consolidation of powder from full melting to sintering conditions, while low fluence enabled a further increase in the formation of porosity.
- **Porosity and pore size versus processing parameters–** The additively manufactured porous structures showed average pore radii and porosity ranging between 9 – 23 µm and 2–42 %, respectively. Thus, the energy density can be tuned to tailor the porosity and pore sizes. Interconnected porosity over the whole structure was maintained and internal wetting surfaces could be exploited for liquid transport.
- **Porosity and pore size versus thermal conductivity–** This paper presented build direction (BD) and scan direction (SD) planes thermal conductivity measurements at room temperature of cubic porous structures with various pore sizes and porosities. The average thermal conductivity of samples with an average porosity of 2.5%–42% was measured as 14 to 6 W/m K, respectively. The effective thermal conductivity of porous structures decreased as porosity was increased and it was found that the simplified series-parallel model and the Misnar model and scaling relation model could approximate the experimental results within an error of 10 and 15 %, respectively.
- **Porosity and pore size versus wetting–** We showed that surface roughness affects the advancing contact angle, which is also dependent on the scan direction and the build direction. Lower contact angles are correlated with rougher surfaces on the build direction of porous structures.

This study provides fundamental knowledge about capillary performance of additively manufactured porous structures. We successfully determined advancing and receding contact angles and reported equilibrium contact angles as well as effective pore radii of such additively manufactured structures. The results are relevant for applications in which heat and mass transfer through additively manufactured porous structures is required. Our results show that careful adjustment of laser power can provide manufacturing conditions allowing to incorporate fully dense structures alongside highly porous features with controlled mass and heat transfer properties within the SLM process. Understanding the relation between manufacturing process parameters, morphological, and thermophysical behaviour will pave the way for the design of next-generation (multiscale) porous media for a wide range of

applications.

CRediT authorship contribution statement

Davoud Jafari: Conceptualization, Formal analysis, Investigation, Methodology, Writing - original draft. **Wessel W. Wits:** Conceptualization, Methodology, Writing - review & editing. **Tom H.J. Vaneker:** Conceptualization, Methodology, Writing - review & editing. **Ali Gökhan Demir:** Conceptualization, Methodology, Writing - review & editing. **Barbara Previtali:** Conceptualization, Methodology, Writing - review & editing. **Bernard J. Geurts:** Conceptualization, Methodology, Writing - review & editing. **Ian Gibson:** Conceptualization, Methodology, Writing - review & editing.

Declaration of Competing Interest

The authors declare that they have no known competing financial interests or personal relationships that could have appeared to influence the work reported in this paper

Acknowledgments

This work was supported by the European Space Agency of The Netherlands (grant number: 4000123341/18/NL/MH).

References

[1] D. Jafari, W.W. Wits, The utilization of selective laser melting technology on heat transfer devices for thermal energy conversion applications: a review, Renew. Sustain. Energy Rev. 91 (2018) 420–442.
[2] Y. Zhang, et al., Review of macroporous materials as electrochemical supercapacitor electrodes, J. Mater. Sci. 52 (19) (2017) 11201–11228.
[3] M.S. Saleh, et al., 3D printed hierarchically-porous microlattice electrode materials for exceptionally high specific capacity and areal capacity lithium ion batteries, Addit. Manuf. 23 (2018) 70–78.
[4] L. Yuan, S. Ding, C. Wen, Additive manufacturing technology for porous metal implant applications and triple minimal surface structures: a review, Bioact. Mater. 4 (1) (2019) 56–70.
[5] I. Gibson, D.W. Rosen, B. Stucker, Additive Manufacturing Technologies, Springer, New York, NY, 2010.
[6] M. Ameli, et al., A novel method for manufacturing sintered aluminium heat pipes (SAHP), Appl. Therm. Eng. 52 (2) (2013) 498–504.
[7] D. Jafari, W.W. Wits, B.J. Geurts, An investigation of porous structure characteristics of heat pipes made by additive manufacturing, 2017 23rd International Workshop on Thermal Investigations of ICs and Systems (THERMINIC) (2017).
[8] D. Jafari, W.W. Wits, B.J. Geurts, Phase change heat transfer characteristics of an additively manufactured wick for heat pipe applications, Appl. Therm. Eng. 168 (2020) 114890.
[9] D. Jafari, W.W. Wits, B.J. Geurts, Metal 3D-printed wick structures for heat pipe application: capillary performance analysis, Appl. Therm. Eng. 143 (2018) 403–414.
[10] J. Esarte, et al., Optimizing the design of a two-phase cooling system loop heat pipe: wick manufacturing with the 3D selective laser melting printing technique and prototype testing, Appl. Therm. Eng. 111 (2017) 407–419.
[11] K.K. Wong, K.C. Leong, Saturated pool boiling enhancement using porous lattice structures produced by Selective Laser Melting, Int. J. Heat Mass Transf. 121 (2018) 46–63.
[12] L.F. Arenas, C. Ponce de León, F.C. Walsh, 3D-printed porous electrodes for advanced electrochemical flow reactors: a Ni/stainless steel electrode and its mass transport characteristics, Electrochem. Commun. 77 (2017) 133–137.
[13] A. Faghri, Heat Pipe Science and Technology, Taylor & Francis, Philadelphia, PA, 1995.
[14] D. Jafari, W.W. Wits, B.J. Geurts, Performance evaluation of an additively manufactured freeform wick for heat pipe applications, 19th International Heat Pipe Conference and 13th International Heat Pipe Symposium (IHPC-IHPS 2018), Pisa, Italy, 2018.
[15] I. Yadroitsev, et al., Manufacturing of fine-structured 3D porous filter elements by selective laser melting, Appl. Surf. Sci. 255 (10) (2009) 5523–5527.
[16] I. Yadroitsev, P. Bertrand, I. Smurov, Parametric analysis of the selective laser melting process, Appl. Surf. Sci. 253 (19) (2007) 8064–8069.
[17] A.G. Demir, P. Colombo, B. Previtali, From pulsed to continuous wave emission in SLM with contemporary fiber laser sources: effect of temporal and spatial pulse overlap in part quality, Int. J. Adv. Manuf. Technol. 91 (5) (2017) 2701–2714.
[18] A.G. Demir, et al., Complementary use of pulsed and continuous wave emission modes to stabilize melt pool geometry in laser powder bed fusion, Opt. Laser Technol. 113 (2019) 15–26.
[19] K. Mumtaz, Top surface and side roughness of Inconel 625 parts processed using selective laser melting, Rapid Prototyp. J. 15 (2) (2009) 96–103.
[20] F. Espana, et al., Influence of porosity and microstructure on thermal properties of laser processed Ni and Ti 6 Al 4 V alloy, Minerals, Metals and Materials Society/AIME, 420 Commonwealth Dr., P. O. Box 430 Warrendale PA 15086 USA (2010).
[21] L.I. Chernyshev, V.V. Skorokhod, Effects of porous structure on the electrical conductivity of highly porous metal-matrix materials, Powder Metall. Met. Ceram. 42 (1) (2003) 88–93.
[22] J. Zhang, et al., Emerging porous materials in confined spaces: from chromatographic applications to flow chemistry, Chem. Soc. Rev. 48 (9) (2019) 2566–2595.
[23] R. Fadida, D. Rittel, A. Shirizly, Dynamic mechanical behavior of additively manufactured Ti6Al4V with controlled voids, J. Appl. Mech. 82 (4) (2015) p. 041004-041004-9.
[24] S.H. Davis, L.M. Hocking, Spreading and imbibition of viscous liquid on a porous base, Phys. Fluids 11 (1) (1998) 48–57.
[25] A.L. Yarin, Drop impact dynamics: splashing, spreading, receding, bouncing…, Annu. Rev. Fluid Mech. 38 (1) (2006) 159–192.
[26] S.H. Davis, L.M. Hocking, Spreading and imbibition of viscous liquid on a porous base. II, Phys. Fluids 12 (7) (2000) 1646–1655.
[27] V.M. Starov, et al., Spreading of liquid drops over dry porous layers: complete wetting case, J. Colloid Interface Sci. 252 (2) (2002) 397–408.
[28] N. Alleborn, H. Raszillier, Spreading and sorption of droplets on layered porous substrates, J. Colloid Interface Sci. 280 (2) (2004) 449–464.
[29] X. Frank, P. Perré, Droplet spreading on a porous surface: a lattice Boltzmann study, Phys. Fluids 24 (4) (2012) 42101.
[30] S. Meng, et al., Simulation of droplet spreading on porous substrates using smoothed particle hydrodynamics, Int. J. Heat Mass Transf. 77 (2014) 828–833.
[31] T. Gambaryan-Roisman, Liquids on porous layers: wetting, imbibition and transport processes, Curr. Opin. Colloid Interface Sci. 19 (4) (2014) 320–335.
[32] A. Clarke, et al., Spreading and imbibition of liquid droplets on porous surfaces, Langmuir 18 (8) (2002) 2980–2984.
[33] J.B. Lee, D. Derome, J. Carmeliet, Drop impact on natural porous stones, J. Colloid Interface Sci. 469 (2016) 147–156.
[34] M. Kaviany, Principles of Heat Transfer in Porous Media, Springer, New York, 1995.
[35] J.K. Carson, et al., Thermal conductivity bounds for isotropic, porous materials, Int. J. Heat Mass Transf. 48 (11) (2005) 2150–2158.
[36] P.G. Collishaw, J.R.G. Evans, An assessment of expressions for the apparent thermal conductivity of cellular materials, J. Mater. Sci. 29 (2) (1994) 486–498.
[37] A. Yegyan Kumar, et al., Impacts of process-induced porosity on material properties of copper made by binder jetting additive manufacturing, Mater. Des. 182 (2019) 108001.
[38] Y.S. Ju, et al., Planar vapor chamber with hybrid evaporator wicks for the thermal management of high-heat-flux and high-power optoelectronic devices, Int. J. Heat Mass Transf. 60 (2013) 163–169.
[39] E. Solórzano, et al., An experimental study on the thermal conductivity of aluminium foams by using the transient plane source method, Int. J. Heat Mass Transf. 51 (25) (2008) 6259–6267.
[40] L. Caprio, A.G. Demir, B. Previtali, Influence of pulsed and continuous wave emission on melting efficiency in selective laser melting, J. Mater. Process. Technol. 266 (2019) 429–441.
[41] A.G. Demir, B. Previtali, Investigation of remelting and preheating in SLM of 18Ni300 maraging steel as corrective and preventive measures for porosity reduction, Int. J. Adv. Manuf. Technol. 93 (5) (2017) 2697–2709.
[42] J. Metelkova, et al., On the influence of laser defocusing in Selective Laser Melting of 316L, Addit. Manuf. 23 (2018) 161–169.
[43] A.G. Demir, et al., Investigation of pulse shape characteristics on the laser ablation dynamics of TiN coatings in the ns regime, J. Phys. D Appl. Phys. 48 (23) (2015) 235202.
[44] A. Gökhan Demir, C. De Giorgi, B. Previtali, Design and Implementation of a multisensor coaxial monitoring system with correction strategies for selective laser melting of a maraging steel, J. Manuf. Sci. Eng. 140 (4) (2018).
[45] M. Amschler, CL 20ES Stainless Steel, (2015).
[46] L.M. Anovitz, D.R. Cole, Characterization and analysis of porosity and pore structures, Rev. Mineral. Geochem. 80 (1) (2015) 61–164.
[47] J. Paek, et al., Effective thermal conductivity and permeability of aluminum foam materials, Int. J. Thermophys. 21 (2) (2000) 453–464.
[48] W. Zhao, et al., Methods for measuring the effective thermal conductivity of metal hydride beds: a review, Int. J. Hydrogen Energy (2020).
[49] C. Shemelya, et al., Anisotropy of thermal conductivity in 3D printed polymer matrix composites for space based cube satellites, Addit. Manuf. 16 (2017) 186–196.
[50] J. Choi, et al., Experimental investigation on sintered porous wicks for miniature loop heat pipe applications, Exp. Therm. Fluid Sci. 51 (2013) 271–278.
[51] M. Nikzad, S.H. Masood, I. Sbarski, Thermo-mechanical properties of a highly filled polymeric composites for fused deposition modeling, Mater. Des. 32 (6) (2011) 3448–3456.
[52] M.A.A. Mendes, et al., Measurement and simplified numerical prediction of effective thermal conductivity of open-cell ceramic foams at high temperature, Int. J. Heat Mass Transf. 102 (2016) 396–406.
[53] G. Laschet, et al., Effective permeability and thermal conductivity of open-cell metallic foams via homogenization on a microstructure model, Comput. Mater. Sci. 45 (3) (2009) 597–603.
[54] N. Yan, et al., Measurement of contact angles for fumed silica nanospheres using enthalpy of immersion data, J. Colloid Interface Sci. 228 (1) (2000) 1–6.
[55] G. Buckton, Contact angle, adsorption and wettability — a review with respect to powders, Powder Technol. 61 (3) (1990) 237–249.
[56] M. Hilpert, A. Ben-David, Infiltration of liquid droplets into porous media: effects of

dynamic contact angle and contact angle hysteresis, Int. J. Multiph. Flow 35 (3) (2009) 205–218.
[57] E. Chibowski, Surface free energy of a solid from contact angle hysteresis, Adv. Colloid Interface Sci. 103 (2) (2003) 149–172.
[58] O. Carrier, D. Bonn, Chapter 2 - contact angles and the surface free energy of solids, in: D. Brutin (Ed.), Droplet Wetting and Evaporation, Academic Press, Oxford, 2015, pp. 15–23.
[59] M.G. Ter Haar, H.T. Becker, Selective laser melting produced Ti-6Al-4V: post-process heat treatments to achieve superior tensile properties, Materials 11 (1) (2018).
[60] A. Ataee, et al., Anisotropic Ti-6Al-4V gyroid scaffolds manufactured by electron beam melting (EBM) for bone implant applications, Mater. Des. 137 (2018) 345–354.
[61] C. Han, et al., Continuous functionally graded porous titanium scaffolds manufactured by selective laser melting for bone implants, J. Mech. Behav. Biomed. Mater. 80 (2018) 119–127.
[62] D. Mahmoud, M.A. Elbestawi, Selective laser melting of porosity graded lattice structures for bone implants, Int. J. Adv. Manuf. Technol. 100 (9) (2019) 2915–2927.
[63] W.M. Lima, et al., The effect of porosity on thermal properties: towards a threshold of particle contact in sintered stainless steel, J. Phys. Condens. Matter 17 (7) (2005) 1239–1249.
[64] J.C. Simmons, et al., Influence of processing and microstructure on the local and bulk thermal conductivity of selective laser melted 316L stainless steel, Addit. Manuf. 32 (2020) 100996.
[65] C. Byon, S.J. Kim, Capillary performance of bi-porous sintered metal wicks, Int. J. Heat Mass Transf. 55 (15) (2012) 4096–4103.
[66] M.R.S. Shirazy, L.G. Fréchette, Capillary and wetting properties of copper metal foams in the presence of evaporation and sintered walls, Int. J. Heat Mass Transf. 58 (1) (2013) 282–291.
[67] A. Faghri, Y. Zhang, 5 - solid-liquid-vapor phenomena and interfacial heat and mass transfer, in: A. Faghri, Y. Zhang (Eds.), Transport Phenomena in Multiphase Systems, Academic Press, Boston, 2006, pp. 331–420.
[68] Y. Lee, et al., Revealing how topography of surface microstructures alters capillary spreading, Sci. Rep. 9 (1) (2019) 7787.
[69] M.A. Quetzeri-Santiago, A.A. Castrejón-Pita, J.R. Castrejón-Pita, The effect of surface roughness on the contact line and splashing dynamics of impacting droplets, Sci. Rep. 9 (1) (2019) 15030.